

1 **Textural changes of graphite by tectonic and hydrothermal**
2 **processes in an active plate boundary fault zone,**
3 **Alpine Fault, New Zealand**

4
5 *Contribution to: Geological Society Special Publication 'Advances in the Characterization of*
6 *Ore-Forming Systems From Geological, Geochemical and Geophysical data' (Editors: Peter*
7 *Sorjonen-Ward, Tom Blenkinsop, and Klaus Gessner)*

8
9 Martina Kirilova^{1*}, Virginia Toy¹, Nick Timms², Timothy Little³, Angela Halfpenny⁴,
10 Catriona Menzies⁵, Dave Craw¹, DFDP-1 Science Team, DFDP-2 Science Team

11
12 ¹Department of Geology, University of Otago, PO Box 56, Dunedin 9054, New Zealand

13 ²Department of Applied Geology, Western Australian School of Mines, Curtin University of Technology, Bentley,
14 Western Australia 6102, Australia

15 ³School of Geography, Environment and Earth Sciences, Victoria University of Wellington, PO Box 600,
16 Wellington 6040, New Zealand

17 ⁴Microscopy and Microanalysis Facility, John de Laeter Centre, Curtin University, Perth, Western Australia 6854,
18 Australia

19 ⁵Ocean and Earth Science, National Oceanography Centre Southampton, University of Southampton,
20 Southampton, SO14 3ZH, United Kingdom

21 *Corresponding author (e-mail: martina.a.kirilova@gmail.com)

22
23 **Abstract**

24 Graphitisation in fault zones is associated both with fault weakening and orogenic gold
25 mineralisation. We examine processes of graphite emplacement and deformation in the Alpine

26 Fault Zone, New Zealand's active continental tectonic plate boundary. Optical and scanning
27 electron microscopic observations reveal a microstructural record of mobilisation of graphite
28 as a function of temperature and ductile then brittle shear strain. Raman spectrometry allowed
29 interpretation of the degree of maturity of carbonaceous material (CM), which reflects thermal
30 and mechanical processes. In the amphibolite-facies Alpine Schist highly crystalline graphite,
31 indicating peak metamorphic temperatures up to 640°C, occurs mainly on grain boundaries
32 within quartzo-feldspathic domains. The subsequent mylonitization process resulted in
33 reworking of CM under lower temperature conditions (500°C – 600°C) in a structurally
34 controlled environment, resulting in clustered (in protomylonites) and foliation aligned CM (in
35 true mylonites). In the brittlely-deformed rocks (cataclasites derived from the mylonitised
36 schists) graphite is most abundant (<50%) and has two different habits: inherited mylonitic
37 graphite and less mature patches of potentially hydrothermal graphite. Tectonic-hydrothermal
38 fluid flow was probably important in deposition of graphite throughout the examined rock
39 sequences. The increasing abundance of graphite may be a significant source of fault
40 weakening, allowing strain localisation, as the fault rocks are progressively exhumed.

41

42 **Keywords**

43 graphite, hydrothermal, tectonic, fault, cataclasite, Raman, Alpine Fault – Deep Fault Drilling
44 Project (DFDP).

45

46 Graphite is a common component of orogenic and Carlin style gold deposits around the world,
47 where it is intimately associated with hydrothermal deposits (Bierlein et al. 2001; Kribeck et al.
48 2008; Large et al. 2007, 2011). Graphite may be inherited from the host rocks, in which case it
49 acts as a chemical reductant that facilitates precipitation of gold and associated sulphide
50 minerals from younger hydrothermal fluids (Cox et al. 1995; Bierlein et al. 2001; Large et al.

51 2007). Graphite may also be added to the mineralising systems as a result of chemical
52 interactions between hydrothermal fluids and the host rocks (Pitcairn et al. 2005; Kribeck et al.
53 2008; Huizenga 2011; Luque et al. 1998, 2009, 2014). Hydrothermal gold deposits are
54 commonly intimately associated with zones of focussed deformation (i. e. the deposits are
55 “structurally controlled”) and graphite derived from both these origins commonly becomes
56 involved in later deformation including fault zone inception and evolution. Graphite is
57 frictionally weak, thus, its presence affects fault mechanics because it can preferentially
58 accommodate localized shear and result in further structurally-controlled mineralization (Binu
59 et al. 2003; Upton & Craw 2008; Oohashi et al. 2011; Kuo et al. 2014; Craw & Upton 2014).
60 For this reason, processes of deformation of graphite in fault zones are of interest in
61 understanding both gold deposits and rheology. Furthermore, flaky crystalline graphite is
62 increasingly recognised as an important mineral resource in its own right (Beysac & Rumble,
63 2014). However, the graphite we have studied is not sufficiently concentrated to present an
64 economically viable resource – a function of the structural setting that we carefully describe
65 here to facilitate future development of realistic models of graphite distribution around various
66 typical geological structures.

67 On a larger scale, the close spatial relationship between graphite and hydrothermal gold deposits
68 can be of relevance for developing exploration strategies in prospective regions. This is because
69 graphite is a highly electrically conductive mineral, and if it forms linked networks it may
70 contribute to a low-resistivity geophysical signal in graphite bearing rocks (Haak & Hutton,
71 1986; Jiracek et al., 2007). Consequently, graphitic rocks and associated graphitic structures
72 can be detected using regional scale geophysical methods such as airborne electromagnetic or
73 magnetotelluric surveys (Won 1983; Gautneb & Tvetin, 2000; Dentith & Barrett, 2003;
74 Heinson et al. 2006; Dentith et al. 2013). The relative roles of conductive fluids versus minerals
75 such as graphite in forming electrically conductive fault zones at depth has been debated by

76 geophysicists interpreting magnetotelluric profiles through major ore-hosting terranes (Wang
77 & Chamalaun, 1996; Heinson et al., 2006; Dentith et al., 2013).

78 Finally, the crystallinity of carbonaceous material (CM) has been calibrated as a
79 geothermometer (Beysac et al., 2002a), that is increasingly employed to understand both P-T
80 evolution of metamorphic zones (Beysac et al., 2016), and to determine fault strength based
81 on estimates of frictional heating that accompanied shear (Kaneki et al., 2016). However,
82 mechanical processes might also modify graphite structure, significantly reducing the accuracy
83 of thermometric estimates.

84 In this study, we document the behaviour of graphite during progressive ductile-to-brittle
85 deformational processes in an active, self-exhuming fault zone in South Island, New Zealand.
86 The most important processes we identify involve both mechanical reworking of inherited
87 graphite in deformed host rocks, and addition of new graphite to fault rocks by
88 syndeformational hydrothermal activity. The fault zone is not known to contain significant gold
89 deposits, although orogenic gold deposits have formed, and are still forming, elsewhere in the
90 hangingwall of the Alpine Fault (Johnstone et al. 1990; Craw et al. 2009; Upton & Craw 2014).
91 Our observations here instead focuss on the various ways in which graphite interacts with an
92 evolving structure, as they were extracted from the active fault zone during recent scientific
93 drilling. We link these observations to inferred processes of formation of orogenic gold deposits
94 in the nearby hangingwall, and in older deposits in the same host rocks including the world-
95 class Macraes orogenic gold mine (Craw 2002; Craw et al. 2009).

96

97 **Geological Setting**

98 *Alpine Fault zone*

99 The oblique-slip Alpine Fault (Fig. 1a) accommodates up to 75% of the 37 mm/yr relative
100 motion at the Australian – Pacific plate boundary, manifest as uplift of the fault hangingwall at
101 $\sim 8 \text{ mm yr}^{-1}$ and dextral strike slip at $27 \pm 5 \text{ mm yr}^{-1}$ (Norris & Cooper, 2001; Herman, et al.,
102 2009). At least 20 km of vertical uplift and exhumation has occurred along the fault, with total
103 strike-separation of $\sim 480 \text{ km}$ (Norris et al., 1990; Norris & Cooper, 1995). The transform plate
104 boundary fault strikes NE-SW and dips at $30 - 50^\circ$ to the SE. At 35 km depth, it soles out into a
105 major crustal decollement (Norris et al., 1990; Norris & Cooper, 1995; Kleffman et al., 1998;
106 Little et al., 2007).

107 Uplift and erosion of the fault zone has exhumed ductile mylonitic rocks from the middle crust,
108 while on-going near-surface deformation continues to form, and rework, cataclasites and
109 gouges which only partially overprint the older, deeper-formed mylonites (Fig. 1b). Thus, rocks
110 formed at the full range of depths over which shearing occurs in the fault zone outcrop at the
111 surface (Fig. 1b; Table 1). The active slip zone is marked by a thin ($< 5 \text{ cm}$) clay gouge layer,
112 forming the base of a 10 to 50 m-thick cataclasite unit composed of crushed angular mylonitic
113 clasts in a fine-grained matrix (Fig. 1b). These brittle rocks are now structurally overlain by a
114 $\sim 1 \text{ km}$ thick mylonite zone (Fig. 1b; Table 1). Based on degree of grain size reduction and
115 transposition of the original protolith fabric, these mylonitic rocks can be subdivided into
116 ultramylonites, mylonites and protomylonites (Toy et al., 2011). This mylonite zone
117 subdivision reflects the relative magnitude of finite ductile shear strain accommodated by those
118 variably foliated and lineated rocks, with increasingly higher strains accommodated nearer to
119 the fault. Most samples were collected on either sub-horizontal or vertical outcrop surfaces or
120 borehole samples. The Alpine Fault and its mylonitic foliation have an average attitude of
121 $055/45 \text{ SE}$ (Norris & Cooper, 2007). The mylonitic foliation is a spaced foliation largely
122 inherited from the protolith amphibolite facies quartzo-feldspathic Alpine Schist, and later (in
123 the Neogene) was cross-cut by extensional (C') shear bands (e.g., Little et al., 2002). The fabric

124 gradually changes from spaced to continuous with increasing proximity to the fault and ductile
125 finite strain magnitude. The protolith is well exposed in the non-mylonitic part of the Southern
126 Alps to the east of the fault zone (Fig. 1b). Farther east the Alpine Schist decreases in
127 metamorphic grade across the Southern Alps mountains, from oligoclase-zone amphibolite
128 facies through garnet, biotite and chlorite zones to pumpellyite-actinolite and prehnite-
129 pumpellyite facies (Little et al., 2005; Cox et al., 2012).

130 *Thermal profile and hydrothermal system*

131 Thermobarometric data from the central Alpine Fault zone, based on garnet-biotite
132 thermometers and garnet-plagioclase barometers in the mylonitic rocks, indicate they
133 equilibrated to P-T conditions of 600–700 °C at 9.2–10 kbar (Table 1; Cooper, 1980; Grapes
134 & Watanabe, 1992; Grapes, 1995). A few kilometres to the south-east of the fault the P-T
135 estimates decrease to 400–540 °C at 4–7 kbar (Cooper, 1980; Grapes, 1995). Recently, Beyssac
136 et al. (2016) determined temperatures in excess of 640 °C close to the Alpine Fault by Raman
137 thermometry. The mineral assemblages in the cataclasites indicate equilibrium at greenschist
138 facies conditions (< 530 °C; Warr & Cox, 2001), however, a pervasive chloritisation occurred
139 under sub-greenschist facies conditions (< 320 °C) and most clay minerals grew at much lower
140 temperatures (<120 °C) (Warr & Cox, 2001).

141 Rapid uplift of hot, tectonically advected rocks along the Alpine Fault has resulted in
142 geothermal gradients of >60 °C km⁻¹ in the upper 3–4 km of the crust, and the brittle-ductile
143 transition (BDT) is inferred to be only be 8–10 km below the surface (Sutherland et al., 2012).
144 Furthermore, a pervasive tectonically-induced fracture network in the fault rocks, together with
145 topographically driven fluid pressure gradients, has allowed meteoric water to penetrate down
146 to at least 6 km depth through this hot rock and to rise again beneath the valleys (Koons, 1987;
147 Koons et al., 1998; Menzies et al., 2014), producing hot springs with temperatures greater than

148 50° C (Barnes et al 1978; Koons, 1987). Isotopic data also suggest metamorphic fluids mingle
149 with meteoric water within this system (Jenkin, 1994; Upton et al., 1995, 2003; Cox et al., 1997;
150 Koons, 1998).

151

152 **Sample Description and Analytical Methods**

153 *Samples*

154 We have examined samples recovered from boreholes that were drilled during the two phases
155 of the Alpine Fault – Deep Fault Drilling Project (DFDP-1A and 1B, and DFDP-2B) (Fig.1).
156 During DFDP-1, undertaken at Gaunt Creek in early 2011, the Alpine Fault was cored in two
157 shallow-depth boreholes, namely DFDP-1A (100.6 m) and DFDP-1B (151.4 m) (Sutherland et
158 al., 2012). Thin sections were prepared from blocks cut perpendicular to the foliation within
159 these cores. In 2014, the DFDP-2B cuttings (chips) were obtained during rotary drilling
160 operations at up to 800 m actual (vertical) depth at Whataroa Valley. These include the non-
161 mylonitic quartz-feldspathic Alpine Schist wall rock, and the Alpine mylonite zone
162 (protomylonites and mylonites). These cuttings thin-sections were prepared from randomly
163 orientated rock chips mounted in resin.

164 For the aims of the current study we used a sample set of 22 thin sections from DFDP-2B,
165 equally distributed with depth, and five DFDP-1 thin sections, representing the principal slip
166 zone of the Alpine Fault, New Zealand. In the current manuscript we present data from samples
167 DFDP-2B 266 (schist), DFDP-2B 518 (protomylonite), DFDP-2B 890 (mylonite), DFDP-1A
168 69.1 (cataclasite) and DFDP-1A 69-2.61 (cataclasite). Sample nomenclature includes the name
169 of the corresponding drilling phase together with the drill depth in meters.

170 *Petrographic methods*

171 Petrographic and microstructural characteristics of the samples were investigated using
172 transmitted and reflected light optical microscopy. Based on these microstructural observations
173 samples with representative graphite were selected for further, more detailed analysis. The
174 structure and composition of the rocks were analysed on TESCAN MIRA3 field emission
175 scanning electron microscope (FESEM) at John de Laeter Centre, Curtin University, Perth,
176 Australia. The instrument was operated at 20 kV using a working distance (WD) of 15 mm.
177 Energy-dispersive X-ray spectroscopy (EDS) maps were collected using an Oxford Instruments
178 X-Max^N 150 mm² silicon drift detector (SDD). The EDS spectra were acquired and processed
179 using Oxford Instruments Aztec software.

180 *Raman Spectrometry of Carbonaceous Material (RSCM)*

181 Raman spectroscopy was performed using a Reinshaw[®] inVia Raman Microscope with a 514
182 gr/mm Spectra Physics argon laser in circular polarization and a Peltier cooled RENCAM CCD
183 detector, located at IMPMC, Paris, France. The laser was focused on the samples by a DMLM
184 Leica microscope with a 100X objective, NA of 0.90 and ND filter of 10 %, producing final
185 laser power of 1 – 2 mW.

186 Raman spectra were collected in the 800 – 1800 cm⁻¹ range in order to capture the first-order
187 region. In order to avoid potential orientation and polishing effects, recognized as the main
188 constraints of RSCM (Beysac et al., 2003b; Beysac & Lazzeri, 2012), we performed only in-
189 depth measurements of carbonaceous material (CM) (Pasteris, 1989) in 30 µm – thick thin
190 sections, orientated as close to perpendicular to the foliation as possible. Because of the nature
191 of the cuttings samples, additional precautions were taken i. e. a quarter waveplate was used to
192 remove potential polarization effects (Beysac & Lazzeri, 2012).

193 Spectra decomposition and analysis were implemented by fitting procedures with the computer
194 program PeakFit. Initially, the baseline was manually corrected by creating splines and

195 removing the background. Afterwards, curves representing Raman bands were fitted with a
196 combination of Lorentzian and Gaussian functions (Voigt profiles), known to yield the best
197 results (Beyssac & Lazzeri, 2012). As an outcome the parameters of the identified peaks were
198 calculated, as well as R1 and R2 ratios (defined below), and the peak metamorphic
199 temperatures.

200

201 **Applications of Raman Spectrometry of Carbonatious Material**

202 Raman spectroscopy has been established as a reliable quantitative method for characterizing
203 the degree of organization of CM. The transformation of organic matter into crystalline graphite
204 is induced by compositional and structural changes during diagenesis and metamorphism,
205 known as graphitization, which is considered to be irreversible. Consequently, characteristics
206 of Raman spectra are used as an indicator of peak metamorphic temperature (Wopenka &
207 Pasteris, 1993; Beyssac et al. 2002a, 2002b, 2004).

208 Fully crystalline graphite consists of hexagonal planes of carbon atoms (space group $D_{6h}^{4} =$
209 $P6_3/mmc$) that result in vibration of E_{2g} in-plane mode, observed as a high frequency Raman
210 peak at $\sim 1580 \text{ cm}^{-1}$ (G band) (Wopenka & Pasteris, 1993). Any disorders or defects in the
211 graphite structure give rise to numerous additional bands, resulting in Raman spectra with first
212 and second-order regions. In the first-order region ($1100\text{--}1800 \text{ cm}^{-1}$), except for the G band,
213 out of plane defects result in the appearance of peaks at $\sim 1350 \text{ cm}^{-1}$ (D1 band) and $\sim 1620 \text{ cm}^{-1}$
214 (D2 band). The D2 band forms a shoulder on the G band (Wopenka & Pasteris, 1993; Beyssac
215 et al. 2002a, 2002b, 2003a, 2003b; Sforza et al., 2014). Very poorly organized CM
216 characteristically has additional bands at $\sim 1500 \text{ cm}^{-1}$ (D3) and $\sim 1150 \text{ cm}^{-1}$, and a shoulder on
217 D1. The second-order region ($2200\text{--}3400 \text{ cm}^{-1}$) is represented by several bands at $\sim 2400,$

218 ~2700 (S1), ~2900 and ~3300 cm^{-1} , associated with overtone and combination scattering
219 (Wopenka & Pasteris, 1993; Beyssac et al. 2002a, 2002b, 2003a, 2003b).

220 Quantification of CM is achieved by decomposition and analysis of the first-order region, more
221 precisely – position, intensity, area (integrated area) and width (full width and half maximum)
222 of the G and D bands (Wopenka and Pasteris, 1993; Beyssac et al. 2002a, 2002b, 2003a, 2003b).
223 Various correlations of these parameters are used to identify the structural order of CM. The
224 most reliable are the intensity ratio between D1 and G bands ($R1=I_{D1}/I_G$) [where I_i = intensity
225 of the i th peak] and the area ratio ($R2=A_{D1}/(A_G+A_{D1}+A_{D2})$) [where A_i = area of the i th peak],
226 introduced by Beyssac et al. in 2002a. Peak temperature in the range 330–650°C can be
227 estimated to $\pm 50^\circ\text{C}$ by the linear correlation $T= - 445R2 + 641$ (Beyssac et al., 2002b).

228

229 **Petrographic Characteristics of the Alpine Fault Rocks**

230 *Alpine Schist*

231 In the amphibolite-facies Alpine Schist there is a grain shape fabric in both quartz and/or
232 feldspar domains and micaceous lamellae parallel to the planar spaced foliation. Large biotite
233 porphyroblasts and garnets are scattered throughout (Fig. 2, Table 1). Quartz grains with mostly
234 irregular, lobate boundaries, show pronounced sweeping undulose extinction, general absence
235 of colour changes on rotation of the stage with the sensitive tint plate inserted (indicating a
236 crystallographic preferred orientation is not present) and average geometric-mean grain size of
237 0.18 mm (based on a linear intercept method as described by Berger et al. (2011). Accessory
238 opaque minerals with tabular habit are ilmenite and pyrrhotite. Graphite occurs as opaque
239 particles at micrometer scale, and it is most commonly distributed on grain boundaries and as
240 inclusions in biotite porphyroblasts (Fig. 3a).

241 *Mylonites*

242 The mylonites and schists have nearly identical modal mineralogies. However, mylonitic
243 rocks have a more uniform quartzo-feldspathic lithology in comparison to the Alpine Schist i.
244 e. the main mineral phases appear as more evenly distributed with less variable grain sizes and
245 shapes in the mylonitic rocks than in the schists. However, the schists` planar foliation is
246 gradually transformed to a wavy and anastomosing foliation then with increasing proximity to
247 the fault a typical macroscopically continuous mylonitic fabric is developed. Throughout the
248 protomylonite sequence shear bands subtend a low angle to the foliation (45° to 15°), and they
249 become increasingly abundant and more closely spaced (spacing ranges from 500 to 145
250 micrometers) in the true mylonite zone (Gillam et al., 2013) (Table 1).

251 In the lowest strain protomylonites (Toy et al., 2012), sampled in the shallower DFDP-2
252 borehole samples, quartz grains show two predominant colours on rotation of the stage with the
253 sensitive tint plate inserted (indicating bimodal distribution) and a geometric-mean ranging
254 from 0.06 to 0.23 mm. Elongated quartz grains (a few hundred micrometers long) with irregular
255 grain shapes, lobate boundaries and undulose extinction form an oblique shape fabric. They are
256 mantled by aggregates of more equant smaller grains with mostly straight grain boundaries and
257 uniform extinction, indicating strain free areas (Norris & Cooper, 2003). In the higher strain
258 mylonites, sampled at greater depths in the DFDP-2 borehole, most quartz grains are smaller
259 (geometric grain size ranging from 0.06 to 0.12 micrometers), more equigranular, and have well
260 defined grain boundaries. Quartz grains show more uniform colours on rotation of the stage
261 with the sensitive tint plate inserted with increasing sample depth, indicating transformation of
262 a weak CPO to a very strong and definite CPO.

263 Fine micaceous material coexists with biotite porphyroblasts, platy muscovite flakes, and mica
264 fish. The biotite porphyroblasts are smaller than the ones observed in the schist rocks, their
265 margins are reworked by the foliation, and there are occasional domino structures. At the
266 protomylonite-mylonite transition, biotite is locally chloritised due to retrogressive

267 metamorphism with this chloritic alteration becoming even more prevalent in the true mylonite
268 section. Also in the transition from protomylonite to mylonite, garnet porphyroblasts become
269 more fractured, with chlorite filling the cracks. These garnet porphyroblasts contain spiralled
270 inclusion trails of the precursor non-mylonitic fabric, and typically have asymmetric strain
271 shadows, but in the true mylonites only fragments of these garnets are found, some of which
272 contain remnants of the inclusion trails. Opaque accessory minerals remain with the same
273 chemical composition and in relatively the same amount as in the schist rocks.

274 *Cataclasites*

275 The cataclasites consist chiefly of intensely crushed mylonites, the fragments of which float in
276 very fine to dusty-grained dark matrix. Asymmetric angular clasts up to 100 μm in size are
277 bounded by a cataclastic foliation, and there is an anastomosing network of dark hairline layers
278 (Table 1). Porphyroclastic quartzo-feldspathic mylonitic fragments, ranging up to a few
279 hundred micrometers in size, are internally fractured with sub-rounded, irregular shapes. These
280 fragments are cemented by a mixture of calcite and clay minerals with significant titanite and
281 graphite, causing dark appearance. These clay minerals are very fine-grained, and some have
282 been identified as illite, kaolinite and chlorite by using XRD in previous studies; kaolinite
283 locally dominates (Warr & Cox, 2001; Boulton et al., 2012; Schleicher et al., 2015). Smectite
284 has been identified in the thin, latest stage fault gouges (Boulton et al., 2012; Schleicher et al.,
285 2015).

286

287 **Graphite Textures**

288 Graphite appears as an accessory mineral throughout the Alpine Schist and mylonite
289 succession. In the amphibolite facies schists, fine-grained single crystals (typically at one

290 micrometer scale or finer) are dispersed mainly along grain boundaries in quartzo-feldspathic
291 domains (Fig. 3a, b). Some randomly oriented graphite inclusions occur within large brown
292 biotite porphyroblasts or in quartz or feldspar domains. Aggregates of graphite grains constitute
293 larger flakes (Fig. 3a, b), which can reach a length up to ~30 μm long. Occasionally,
294 concentrations of graphite appear as elongated seams along grain boundaries (Fig. 3b).

295 In the mylonitic rocks, graphite persists with similar grain size to that in the metamorphic
296 protoliths. In the protomylonite section, clusters of graphite grains commonly occur within
297 silicate minerals, especially quartz and feldspar. These appear to have formed by aggregation
298 of the once more dispersed graphite grains that typify the protolith schists (Fig. 3c, d). In the
299 mylonites, graphite grains are also clustered into aggregates that are broadly aligned with the
300 foliation (Fig. 3e, f). In contrast to the non-mylonitic rocks, in the mylonites graphite is most
301 abundant at grain and sub-grain boundaries of recrystallised quartzo-feldspathic domains (Fig.
302 3c, f), but we also observed dusty graphitic concentrations that are spatially associated with
303 iron oxides (Fig. 3c, d), especially in the protomylonites. Graphite inclusions are rare in remnant
304 biotite porphyroblasts. Phyllosilicate minerals are commonly aligned with fine-grained
305 graphite, and recrystallized matrix material (Fig. 3e, f). In Fig. 3e, an ilmenite porphyroclast
306 has inclusions of graphite grains parallel to the old metamorphic foliation, and other graphite
307 grains are aligned along the overprinting mylonitic foliation.

308 In the cataclastic rocks, mylonitic clasts enveloped by the cataclastic matrix preserve some of
309 the pre-existing mylonitic fabric, and have graphite textures identical to those described above.
310 In addition, the cataclastic matrix is locally filled and cemented by fine grained graphite
311 (approximately one micrometer across). This graphite generally aggregated to form larger
312 graphitic patches (a few hundred micrometers across) in the cataclasites, which locally
313 constitute ~50% of the rock volume (Fig. 4a-e). On a thin section scale, some of these

314 aggregates are aligned as part of an anastomosing network of dark-coloured shear surfaces
315 decorated by slickensides (Fig. 4f).

316

317 **Graphite Crystallinity and Raman Thermometry**

318 *Raman spectra*

319 Raman spectra acquired from graphitic grains in the Alpine Fault rocks show typical G and D1
320 bands, respectively at $\sim 1580\text{ cm}^{-1}$ and $\sim 1350\text{ cm}^{-1}$, which allowed us to analyse the degree of
321 crystallinity in the CM (Fig. 5). In schist (Fig. 5a) and mylonite samples (Fig. 5b, c) D1 bands
322 show low intensity in comparison with the G bands (Fig. 5), and correspondingly low and
323 relatively consistent R1 values (between 0.02 and 0.26), suggesting well-organized graphite
324 with slight structural variations throughout the successions. The overall spectra analysis shows
325 that the schist CM material has achieved slightly higher maturity in comparison with the
326 mylonite zone (Fig. 5 a, b, c).

327 In contrast, R1 in the examined cataclasites (Fig. 5d, e, f) ranges between 0.13 and 0.8,
328 indicating significant variations in the graphite structures. Highly mature graphite, showing
329 identical spectra with the mylonite samples (Fig. 5d), was identified in preserved mylonitic
330 porphyroclasts. Simultaneously, the dusty graphite aggregates and veins appear to be composed
331 of less organized CM (in comparison with CM in schist and mylonite rocks) with variable
332 degree of maturity (Fig. 5e, f). In graphitic patches spectra comparable with the mylonitic CM
333 (Fig. 5e) coexist with spectra showing extremely high D1 peaks (Fig. 5f), indicating very poorly
334 organized CM is present.

335 *RSCM thermometry*

336 From the Raman spectra we are able to estimate the temperature conditions in the Alpine Fault
337 rocks, based on the R2 ratio values. We estimate peak metamorphic temperatures up to 640° C
338 with maximum error of $\pm 50^\circ$ C in the non-mylonitic amphibolite facies schist (Fig. 5a).
339 Estimated temperatures in the mylonites are slightly lower (between 500° C and 600° C).
340 However, the Raman-based geothermometry method relies on progressive maturation of
341 originally organic CM (Beyssac et al. 2002a, b; 2003). Hence, application of this
342 geothermometry method in the deformed Alpine Fault rocks may not be valid because of
343 possible recrystallisation of the CM (see discussion below). Similarly, temperature estimates in
344 the cataclasites could indicate a range of 400 - 500°C (Fig. 5d), but these temperature estimates
345 have no real meaning if the CM has been recrystallised.

346

347 Discussion

348 *Deformation of metamorphic graphite*

349 Graphite associated with the Alpine Fault zone manifests itself as very fine (1 to 5 microns) to
350 dusty grains, arranged in a variety of textures and crystallinity, as a result of ongoing
351 metamorphic and deformation-related processes. Initially, metamorphic graphite has grown
352 predominantly on grain boundaries in the Alpine Schist, where RSCM thermometry indicates
353 temperatures typical for amphibolite facies metamorphism – up to $640 \pm 50^\circ$ C (Cooper, 1980;
354 Grapes & Watanabe, 1992; Grapes, 1995, Toy et al., 2010, Beyssac et al., 2016). The
355 subsequent mylonitization of the schist rock resulted in partial recrystallisation of the rock
356 volume under slightly lower temperatures (500 – 600° C from RSCM thermometry), which
357 coincide with previous temperature estimates in the Alpine Fault mylonites (Toy, et al., 2010).
358 Under these conditions, remobilisation of CM apparently took place, and graphite with lower
359 maturity (in comparison with the schist protolith) was redeposited in quartzo-feldspathic

360 domains in structurally controlled settings. Previous observations on graphite textures in
361 greenschist facies and at lower metamorphic grade schists, in equivalent non-mylonitic schists
362 further to the east of the Southern Alps, have identified graphite in close association with
363 metamorphic micaceous minerals (Craw 2002; Henne & Craw, 2012; Hu et al. 2015). However,
364 our study demonstrates that graphite mainly occurs within, or along grain boundaries of
365 quartzo-feldspathic domains, both in the protolith schists and in the mylonitic rocks (Fig. 3).
366 The principal exceptions are the graphitic inclusions in relict biotite porphyroblasts, which are
367 progressively reworked and recrystallised with increasing strain (Toy et al. 2010).

368 In the cataclasites, our Raman data and textural observations (Fig. 4, 5) show that two highly
369 crystalline graphite types with non-identical crystallinity and distribution coexist, indicating
370 two structurally different generations of graphite. The first generation of graphite, preserved in
371 remnants of mylonitic clasts, carries the textural and crystallographic arrangement of graphite
372 in the mylonitic rocks (Fig. 4b, c). In contrast, the second generation of graphite has been
373 accumulated in the cataclastic matrix and in slickenside-rich shear surfaces, forming localised
374 graphite enrichment (Fig. 4). The first generation of graphite is clearly inherited from mylonitic
375 rocks, and the graphite textures or Raman signals of this generation have not been significantly
376 affected by cataclasis.

377 The abundance and textures of the second generation of graphite that occurs in the cataclasite
378 matrix supports observations on the silicate matrix that there has been extensive fluid-driven
379 modification in these rocks (Boulton et al., 2012). Locally abundant CM in these rocks (Fig. 4)
380 may result from either residual concentration during extensive dissolution of the silicate matrix,
381 or hydrothermal addition of graphite by the alteration fluids (Beysac & Rumble, 2014; Galvez
382 et al., 2013a, b). Without detailed microchemical analyses of these CM-bearing rocks,
383 distinguishing these possibilities is difficult. However, petrographic observations of the

384 cataclasites show that while the metamorphic silicates have been variably transformed to
385 aluminous clay minerals, there has not been an associated residual increase in relatively
386 insoluble minerals such as zircons in the vicinity of the matrix CM. Further, the matrix CM has
387 a distinctly different Raman signal from that of the parent amphibolite facies schists and
388 mylonites (Fig. 5). On the basis of these observations, we tentatively conclude that the matrix
389 CM was added to the rocks hydrothermally. Similar interpretations have also been made in
390 other fault zones, such as Annapurna Himal, Central Nepal (Craw & Upton, 2014) and Hidaka
391 metamorphic belt, Hokkaido, Japan (Nakamura et. al, 2015). More conclusive demonstration
392 of the formation of hydrothermal graphite in these rocks remains a goal for future research.

393 The variations in the crystallographic order of the second generation of graphite can also
394 signify hydrothermal graphite formation by consecutive pulses of fluids with variable
395 temperatures. However, we also acknowledge the possibility of amorphization of CM as a result
396 of intense shear deformation (Nakamura et al., 2015). There is evidence in our samples for
397 deformation of the graphite pools into elongate shears within the cataclasite (Fig. 4), but we
398 have no local, high resolution RSCM data to provide evidence for amorphization in these
399 shears. Nevertheless, the sheared graphite may weaken these parts of the cataclasites, and
400 causes further strain accommodation along localised slip surfaces, as modelled by Upton and
401 Craw (2008).

402 *Hydrothermal alteration of cataclasite*

403 The alteration of sub-amphibolite facies protoliths (Fig. 1b) to the lower metamorphic grade
404 mineral assemblages commonly documented in the cataclasite sequence is due to fluid-rock
405 interaction across a range of temperatures as the fault rocks have been exhumed up the Alpine
406 Fault. Deformation-driven, episodic enhancement of permeability facilitated hydrothermal
407 fluids flowing in the hangingwall to penetrate the lower permeability fault zone and infill

408 fractures and pore spaces with secondary minerals. This resulted in multiple generations of
409 alteration and precipitation of secondary minerals in the fault zone over a range of temperatures
410 (Table 1). Chloritic alteration can occur at temperatures up to 320–360 °C (Warr & Cox, 2001).
411 Fluid inclusion microthermometry yields estimates of precipitation temperatures of deformed
412 quartz veins containing chlorite of 325 ± 15 °C (Toy et al. 2010; Menzies et al., 2014). The
413 temperatures at which the documented secondary minerals may precipitate from fluids with the
414 chemical composition of local spring waters from the hangingwall hydrothermal system (Reyes
415 et al., 2010) can be estimated by calculating the saturation indices of the secondary minerals in
416 the fluid using PHREEQC and the Ilnl database (Parkhurst & Appelo, 1999). These calculations
417 (Parkhurst & Appelo, 1999) indicate that the mineral assemblage may be near equilibrium with
418 hot spring waters at ~90–100 °C (Fig. 6), which represents the latest stage mineralisation of
419 the fault zone. The hydrothermally altered cataclasite matrix is dominated by the latter minerals,
420 which co-exist with the CM in the matrix. We infer that hydrothermal precipitation of graphite,
421 if such did occur, was an accompaniment of this lower temperature alteration process (Fig. 6,
422 7).

423 *Significance of hydrothermal graphite addition*

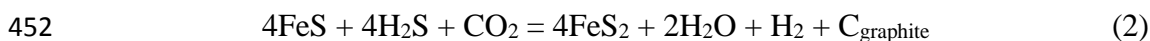
424 Our preliminary conclusion in the previous section that there has been hydrothermal graphite
425 addition to the cataclasites raises some important structural and geochemical issues. Open
426 fractures in brittlely deformed cataclasites induce high permeability potentially allowing high
427 temperature fluids to be transported from middle to lower crust during earthquake events
428 (Oohashi et al., 2011). If graphite precipitates from these fluids, further fault rock weakening
429 and lubrication of fault movements may occur, creating more permeability, and additional
430 deposition of graphite (Upton & Craw, 2008). Carbon-bearing fluids with both meteoric and
431 metamorphic origins propagate through the Alpine Fault rocks (Jenkin, 1994; Upton et al.,
432 1995; Upton & Craw, 2003; Cox et al., 1997; Menzies et al., 2014). Meteoric waters dominate

433 in the Southern Alps hydrothermal system right down to the brittle-ductile transition (Menziez
 434 et al. 2014) and therefore dominates in the cataclastic zone. These fluids contain both carbon
 435 dioxide and methane (Barnes et al. 1978), although CH₄ is subordinate to CO₂ (Jenkin et al.
 436 1994).

437 Previous studies from greenschist-facies schist to the east of the Southern Alps (with similar
 438 composition to Alpine Schist) suggest that hydrothermal precipitation of graphite resulted from
 439 mixing of CO₂ and CH₄ fluids during Mesozoic metamorphism (Craw, 2002; Henne & Craw,
 440 2012). Graphite deposition from a C – O – H bearing fluid is inevitable below 400 °C, because
 441 CO₂ and CH₄ at these temperatures can coexist in very small amounts only (Holloway 1984;
 442 Craw 2002; Huizenga 2011). Hydrothermal graphite can be deposited under these conditions
 443 via the reaction:



445 This process may also be occurring in the modern Alpine Fault zone. However, the relative
 446 scarcity of CH₄ in the Alpine Schist fluids suggests that some additional reactions may be
 447 occurring, involving reduction of the abundant CO₂. A small but significant amount of
 448 pyrrhotite in the Alpine Schists is being transformed to pyrite during uplift, and this pyrite is
 449 widespread in the cataclasites (Fig. 2; Johnstone et al. 1990). This sulphide mineral
 450 transformation involves oxidation of sulphur, and coeval reduction of CO₂ to graphite may
 451 occur as part of this process, perhaps according to the following reactions (Fig. 7):



454 Retrogressive or hydrothermal chlorite in the cataclasites (Fig. 2) is the most likely recipient of
 455 the FeO component in Equation 3. Irrespective of the actual reaction(s) involved, our

456 observations provide firm evidence that hydrothermal graphite is being deposited under near-
457 greenschist facies conditions in the Alpine Fault zone cataclasites.

458 We also have evidence for transformation of fine grained metamorphic graphite under ductile
459 conditions at depth within the mylonitic zone of the Alpine Fault (Fig. 3). Dusty graphite along
460 grain boundaries in amphibolite facies Alpine Schist coincides with the principal fluid flow
461 permeability along grain boundaries in these rocks (Craw & Norris 1993). Hence, it is likely
462 that at least some recrystallisation of metamorphic graphite has occurred, to emplace that
463 graphite along grain boundaries. Furthermore, this dusty graphite becomes concentrated into
464 clusters within the silicate minerals as they recrystallise in the mylonitic rocks nearer to the
465 Alpine Fault (Fig. 3), which implies further remobilisation and recrystallisation of graphite. The
466 scale of these remobilisation and recrystallisation processes may be small (micrometers to
467 millimetres), but they are sufficient to completely transform the metamorphic graphite textures
468 (Fig. 3). Since these amphibolite facies rocks were pervaded by CO₂-bearing fluid, with minor
469 CH₄ (Craw & Norris 1993; Jenkin et al., 1994), the graphite formation probably occurred via
470 Equation 1 (Fig. 7). However, CO₂ and CH₄ can coexist in higher concentrations under
471 amphibolite facies conditions than in greenschist facies fluids (Holloway, 1984; Huizenga,
472 2011). Hence, the graphite formation process probably involved Equation 1 operating in both
473 directions, resulting in localised remobilisation with no net increase in graphite contents of these
474 rocks.

475 *Significance for conductive geophysical signals*

476 Magnetotelluric surveys in the central section of the Southern Alps demonstrate the existence
477 of a high-conductivity zone in the mid-crust (at ~8 km depth), coinciding with the down-dip
478 projection of the Alpine Fault (Wannamaker et al., 2002; Caldwell et al., 2012, 2013). This
479 zone has been interpreted as a ductile shear zone, perhaps resulting from the presence of fluid

480 or interconnected graphite. The topic is of particular interest because the conductive zone in the
481 ductile lower crust underlays the seismogenic zone of the Alpine Fault. Thus, a relationship
482 between the two has been inferred and it was assumed that seismic events in the brittle zone
483 might be triggered by stress response or fluid escape from the underlying ductile zone
484 (Wannamaker et al., 2002; Caldwell et al., 2012, 2013).

485 The electrically conductive zone is relevant to the current study because of the potential role of
486 graphite. Wannamaker et al. (2002) argued it is unlikely that interconnected graphite remains
487 structurally coherent at greater depth and suggested that a combination of fluid and graphite is
488 more likely to be the reason for the presence of highly conductive zone. But convincing
489 evidence has not yet been documented for either of these cases. We observed locally connected
490 dusty graphite at slickensided surfaces in the Alpine Fault cataclasites (Fig. 5f), but we do not
491 have evidence that this graphite occurs on a larger scale, or could be preserved under ductile
492 conditions.

493 *Significance for gold mineralisation processes*

494 Orogenic gold deposits in ancient metamorphic belts have formed from some combination of
495 metamorphic, magmatic and meteoric fluids, and are typically hosted in greenschist facies rocks
496 (Cox et al. 1995; Groves et al. 2003; Goldfarb et al. 2005; Large et al. 2011). The active
497 hydrothermal system in the Southern Alps of New Zealand provides a modern analogue for
498 many components of orogenic gold emplacement systems (Johnstone et al. 1990; Craw et al.
499 2009; Upton & Craw 2014; Pitcairn et al. 2014). Beneath the Southern Alps, metamorphic
500 transformation from greenschist to amphibolite facies is releasing water, Au, As, and related
501 metals from the rocks into the orogen-scale hydrothermal system, to be emplaced as small gold
502 deposits at shallower levels (Craw et al. 2009; Upton & Craw 2014; Pitcairn et al. 2014). There

503 is no associated modern-day magmatism, and the mineralising hydrothermal fluid is a mixture
504 of metamorphic and meteoric water (Craw et al. 2009; Pitcairn et al. 2014; Menzies et al. 2014).

505 Some of the gold deposits in the hangingwall of the Alpine Fault are localised in graphitic
506 greenschist facies schists, and the metamorphic graphite has apparently been responsible for
507 facilitating reductive deposition of sulphide minerals and gold (Craw et al. 2009). However, no
508 previous evidence has been found in any of the hydrothermal deposits for hydrothermal graphite
509 deposition, with or without gold. The present study provides the first tentative evidence for
510 hydrothermal graphite deposition in near-greenschist facies conditions from mixed
511 metamorphic and meteoric fluids of the Alpine Schist active hydrothermal system. As yet, we
512 have no evidence for coeval gold deposition associated with this hydrothermal graphite.
513 However, our inference of the emplacement of hydrothermal graphite in the Alpine Fault
514 cataclasites provides yet another component to the Southern Alps hydrothermal system as an
515 analogue for ancient orogenic gold deposit formation processes.

516 The world-class Macraes orogenic gold mine (Craw 2002) is located east of the Southern Alps
517 and is hosted in lower greenschist facies rocks, equivalent to, but of lower metamorphic grade
518 than, the Alpine Schist described above. This deposit formed in a shear zone during uplift from
519 ductile to brittle conditions in the latter stages of Mesozoic deformation and metamorphism. A
520 distinctive feature of this deposit is the abundant hydrothermal graphite that was added to the
521 shear zone during gold mineralisation (Craw 2002; Pitcairn et al. 2005; Hu et al. 2015).
522 Deformation, fluid flow, and mineralisation were all facilitated by this hydrothermal graphite
523 addition, and the graphite therefore contributed to the large scale of the mineralisation in the
524 hosting structure (Craw 2002; Upton & Craw 2008). Our Alpine Fault observations show that
525 similar metamorphic-hydrothermal graphite recrystallisation, emplacement, and subsequent
526 deformation is occurring under near-greenschist facies conditions as these rocks are uplifted
527 from ductile to brittle conditions.

528

529 **Conclusions**

530 We have documented the crystallinity and microstructural occurrence of graphite in the active
531 Alpine Fault zone as a function of varying temperature and shear strain magnitude. Our study
532 demonstrates that ongoing deformation processes and hydrothermal fluid flow resulted in
533 deposition of graphite with different textural and structural characteristics throughout the
534 examined rock sequences. Highly crystalline graphite, carried by the non-mylonitic
535 amphibolite-facies Alpine Schist rocks, has apparently recrystallized during mylonitization of
536 the metamorphic protolith. Brittle cataclasis associated with tectonic movements along the fault
537 zone allowed penetration of C-bearing hydrothermal fluids. These fluids have extensively
538 altered the silicates in the cataclasites and may have deposited hydrothermal graphite. We
539 identified two coexisting generations of graphite in the Alpine Fault cataclasites on the basis of
540 petrographic textures and Raman signals: (i) inherited graphite, in remnants of mylonitic clasts
541 that carry the textural arrangement of mylonitic graphite; and (ii) less crystalline graphite which
542 has accumulated in large dusty aggregates in the hydrothermally altered matrix of the
543 cataclasites. RSCM thermometry of CM indicates peak metamorphic temperatures in the parent
544 amphibolite facies schists consistent with previous studies in samples, representing the Alpine
545 Schist and mylonite rocks. However, CM in the Alpine Fault cataclasites has a distinctly
546 different Raman signal from that of the parent rocks, and we infer a hydrothermal origin for
547 that material. Hydrothermal deposition of graphite in the fault zone may cause structural
548 weakening if connected on a significant scale. Connected graphite could also result in higher
549 electrical conductivity in a fault zone, enhancing a magnetotelluric signal.

550

551 **Acknowledgement**

552 The research was funded by the University of Otago, New Zealand. We would like to
553 acknowledge the contribution of all members of DFDP-1 and DFDP-2 Science Teams. The
554 authors acknowledge the use of Curtin University's Microscopy & Microanalysis Facility,
555 whose instrumentation has been partially funded by the University, State and Commonwealth
556 Governments of Australia. We also wish to thank our colleague Olivier Beyssac for generously
557 offering us to use the Raman microspectrometer lab at IMPMC, Paris, France, and for valuable
558 discussions and helpful comments during the acquisition, processing and interpretation of
559 Raman data.

560

561 **Table captions**

562 *Table 1* – Summary of petrographic and microstructural observations, and Raman data interpretations
563 in the Alpine Fault rocks.

564

565 **Figure captions**

566 *Figure 1* - (a) Tectonic setting of New Zealand, with the plate boundary, which is the Alpine
567 Fault trace through the South Island, delineated by bold black line. Bathymetric map compiled
568 by the National Institute of Water and Atmospheric Research of New Zealand. Red square
569 indicates the study area.(b) Schematic cross section of typical Alpine Fault rock sequence,
570 modified after Norris and Cooper (2007).

571 *Figure 2* - Paragenetic diagram showing the distribution of mineral phases in the different
572 Alpine Fault rock types. The diagram was created for the purpose of the current study.

573 *Figure 3* - Backscattered SEM images of polished thin sections showing typical graphite
574 textures in the Alpine Fault rocks. (a), (b) schist; (c), (d) protomylonite; and (e), (f) mylonite.

575 Dark material labeled 'Gr' is graphite. White materials are labelled with Ox for oxide and Ilm
576 for ilmenite

577 *Figure 4* - Backscatter SEM images of polished thin sections of cataclasites from the Alpine
578 Fault zone. Dark material labeled 'Gr' is graphite. It occurs either as pools (c), veins (a), or
579 cements (b, d, e); or (f) seams we infer are equivalent to slickensided shear surfaces observed
580 on rock chips.

581 *Figure 5* - Representative Raman spectra of graphite from the different types of Alpine Fault
582 rocks.

583 *Figure 6* – Schematic diagram illustrating the temperatures of the the secondary minerals
584 estimated by calculating the saturation indices of these minerals in the fluid using PHREEQC
585 and the Ilnl database (Parkhurst & Appelo, 1999).

586 *Figure 7* – Schematic diagram illustrating the conditions under which we infer graphite is
587 precipitated in the Alpine Fault zone. The diagram was created for the purpose of the current
588 study.

589

590 **References**

591 Barnes, I., Downes, C.J. & Hulston, J.R. 1978. Warm springs, South Island, New Zealand, and
592 their potential to yield laumontite. *American Journal of Science* 278, 1412–1427.

593 Berger, A., Herwegh, M., Schwarz, J. O. & Pultiz, B. 2011. Quantitative analysis of
594 crystal/grain sizes and their distributions in 2D and 3D. *Journal of Structural Geology* vol. 33
595 (12) pp. 1751-1763

596 Beyssac, O., Goffe', B., Chopin, C. & Rouzaud, J. N. 2002a. Raman spectra of carbonaceous
597 material in metasediments: a new geothermometer. *Journal of Metamorphic Geology*, 20, 859–
598 871.

- 599 Beyssac, O., Rouzaud, J.-N., Goffe', B., Brunet, F. & Chopin, C. 2002b. Graphitization in a
600 high-pressure, low-temperature metamorphic gradient: a Raman microspectroscopy and
601 HRTEM study. *Contributions to Mineralogy and Petrology*, 143, 19–31.
- 602 Beyssac, O., Goffe', B., Petitet, J.-P., Froigneux, E., Moreau, M. & Rouzaud, J.-N. 2003a. On
603 the characterization of disordered and heterogeneous carbonaceous materials by Raman
604 spectroscopy. *Spectrochimica Acta Part A: Molecular and Biomolecular Spectroscopy*, 59,
605 2267–2276.
- 606 Beyssac, O., Brunet, F., Petitet, J.P., Goffe', B. & Rouzaud, J.N. 2003b. Experimental study of
607 the microtextural and structural transformations of carbonaceous materials under pressure and
608 temperature. *European Journal of Mineralogy*, 15, 937–951.
- 609 Beyssac, O., Bollinger, L., Avouac, J.-P. & Goffe', B. 2004. Thermal metamorphism in the
610 lesser Himalaya of Nepal determined from Raman spectroscopy of carbonaceous material.
611 *Earth and Planetary Science Letters*, 225, 233–241.
- 612 Beyssac, O & Lazzeri, M. 2012. Application of Raman spectroscopy to the study of graphitic
613 carbons in the Earth Sciences. *EMU Notes in Mineralogy*, Vol. 12, Chapter 12, 415–454
- 614 Beyssac, O & Rumble, D. 2014 Graphitic Carbon: A Ubiquitous, Diverse, and Useful
615 Geomaterial. *Element. An International Magazine of Mineralogy, Geochemistry and Petrology*.
616 Vol. 10, p. 415-420, doi:10.2113/gselements.10.6.415
- 617 Beyssac, O., Cox, S., Vry, J., Herman, F. 2016. Peak metamorphic temperatures and thermal
618 history of the Southern Alps (New Zealand). *Tectonophysics*, doi:10.1016/j.tecto.2015.12.024

- 619 Bierlein F.P., Cartwright I. & McKnight S. 2001. The role of carbonaceous “indicator” slates
620 in the genesis of lode gold mineralization in the western Lachlan Orogen, Victoria, southeastern
621 Australia. *Econ Geol* 96: 431-451
- 622 Binu, L.S.S., Kehelpannala, K.V.W., Satish, K.M. & Wada, H. 2003. Multistage graphite
623 precipitation through protracted fluid flow in sheared metagranitoid, Digana, Sri Lanka:
624 evidence from stable isotopes. *Chemical Geology*, v. 197, p. 253-270.
- 625 Boulton, C., Carpenter, B.M., Toy, V. & Marone, C. 2012. Physical properties of surface
626 outcrop cataclastic fault rocks. *Geochem. Geophys. Geosyst.*, 13, Q01018,
627 doi:10.1029/2011GC003872
- 628 Caldwell, T.G., Bannister, S., Bourguignon, S., Hill, G.J., Bertrand, E.A., Bennie, S., L.,
629 Heisel, W., Ogawa, Y. & Bibby, H.M. 2012. EQC project ‘Electrical conductivity structure of
630 the Alpine Fault and its relationship to seismicity and seismogenesis’.
- 631 Caldwell, T.G., Heise, W., Ogawa, Y., Hill, G.J., Bertrand, E., A., Bennie, S.L., Bibby, H.M.
632 & Jiracek, G.R 2013. Electrical conductivity structure of the Alpine Fault, New Zealand – a 3D
633 anisotropic problem. *5th International Symposium on Three-Dimensional Electromagnetics*,
634 *Sapporo, Japan, May 7-9, 2013.*
- 635 Cooper, A.F. 1980. Retrograde alteration of chromian kyanite in metachert and amphibolite
636 whiteschist from the Southern Alps, New Zealand, with implications for uplift on the Alpine
637 Fault: *Contributions to Mineralogy and Petrology*, v. 75, p. 153–164,
638 doi:10.1007/BF00389775.
- 639 Cox, S.F., Sun, S-S., Etheridge, M.A., Wall, V.J., & Potter, T.F. 1995. Structural and
640 geochemical controls on the development of turbidite-hosted gold quartz vein deposits, Wattle
641 Gully mine, central Victoria, Australia. *Economic Geology*, v. 90, p. 1722-1746.

- 642 Cox, S. C., Craw, D. & Chamberlain, C. P. 1997. Structure and fluid migration in a late
643 Cenozoic duplex system forming the Main Divide in the central Southern Alps, New Zealand.
644 *New Zealand Journal of Geology and Geophysics*, 40, 359–373.
- 645 Cox, S.C., Stirling, M.W., Herman, F., Gerstenberger, M. & Ristau, J. 2012. Potentially active
646 faults in the rapidly eroding landscape adjacent to the Alpine Fault, central Southern Alps, New
647 Zealand. *Tectonics*, 31, TC2011.
- 648 Craw, D. & Norris, R.J. 1993. Grain boundary migration of water and carbon dioxide during
649 uplift of garnet-zone Alpine Schist, New Zealand. *Journal of Metamorphic Geology* 11: 371-
650 378.
- 651 Craw, D. 2002. Geochemistry of late metamorphic hydrothermal alteration and graphitisation
652 of host rock, Macraes gold mine, Otago Schist, New Zealand. *Chem Geol* 191: 257-275.
- 653 Craw, D., Upton, P. & MacKenzie, D.J. (2009) Hydrothermal alteration styles in ancient and
654 modern orogenic gold deposits, New Zealand. *New Zealand Journal of Geology and*
655 *Geophysics* 52: 11-26.
- 656 Craw, D. & Upton P. 2014. Graphite reaction weakening of fault rocks, and uplift of the
657 Annapurna Himal, central Nepal. *Geosphere* 10: 720-731.
- 658 Dentith, M. & Barrett, D. 2003. Geophysical exploration for graphite at Uley, South Australia.
659 *ASEG Special Publications* (3) 47 - 57
- 660 Dentith, M., Evans, S., Thiel, S., Gallardo, L., Joly, A. & Romano, S. (2013) A magnetotelluric
661 traverse across the southern Yilgarn Craton. *Geological Survey of Western Australia Report*
662 121, 43 pp.

- 663 Galvez, M., Beyssac, O., Martinez, I., Benzerara, K., Chaduteau, C., Malvoisin, B. &
664 Malavieille, J. 2013a. Graphite formation by carbonate reduction during subduction. *Nature*
665 *geoscience*, doi:10. 1038/NGEO1827
- 666 Galvez, M., Martinez, I., Beyssac, O., Benzerara, K., Agrinier, P. & Assayag, N. 2013b.
667 *Contrib Mineral Petrol* 166:1687–1708, doi:10.1007/s00410-013-0949-3
- 668 Gautneb H. & Tveten E. 2000. The geology, exploration and characterisation of graphite
669 deposits in the Jennestad area, Vesterålen, northern Norway. *NGU Bulletin* 436: 67-74.
- 670 Gillam, B. G., Little, T., A., Smith, E. & Toy, V., G. 2013. Reprint of Extensional shear band
671 development on the outer margin of the Alpine mylonite zone, Tatara Stream, Southern Alps,
672 New Zealand. *Journal of Structural Geology*, Volume 64, July 2014, Pages 115-134
- 673 Goldfarb, R.J., Baker, T., Dube, B., Groves, D.I., Hart, C.J. & Gosselin, P. 2005. Distribution,
674 character and genesis of gold deposits in metamorphic terranes. In: Hedenquist, J.W.,
675 Thompson, J.F.H., Goldfarb, R.J., Richards, J.P., (Eds.), *Economic Geology* 100th Anniversary
676 Volume, 407-450.
- 677 Grapes, R.H. & Watanabe, T. 1992. Metamorphism and uplift of Alpine Schist in the Franz
678 Josef– Fox area of the Southern Alps, New Zealand: *Journal of Metamorphic Geology*, v. 10,
679 p. 171–180, doi:10.1111/j.1525-1314.1992.tb00077.x.
- 680 Grapes, R. H. 1995. Uplift and exhumation of Alpine Schist, Southern Alps, New Zealand:
681 thermobarometric constraints. *New Zealand Journal of Geology & Geophysics*, 38, 525–533.
- 682 Groves, D.I., Goldfarb, R.J., Robert, F. & Hart, C.J. 2003. Gold deposits in metamorphic belts:
683 overview of current understanding, outstanding problems, future research, and exploration
684 significance. *Economic Geology* 98, 1-29.

- 685 Haak, V. & Hutton, R. 1986. Electrical resistivity in continental lower crust, in Nature of Lower
686 Continental Crust *Geological Society Special Publications*, 24, 35– 49
- 687 Heinson, G. S., Direen, N. G. & Gill, R. M. 2006. Magnetotelluric evidence for a deep-crustal
688 mineralizing system beneath the Olympic Dam iron oxide copper-gold deposit, southern
689 Australia. *Geology* 34: 573-576.
- 690 Henne, A. & Craw, D. 2012. Synmetamorphic carbon mobility and graphite enrichment in
691 metaturbidites as a precursor to orogenic gold mineralization, Otago Schist, New Zealand.
692 *Mineralium Deposita*, v. 47, p. 781-797.
- 693 Herman, F., Cox, S. C. & Kamp, P. J. J. 2009. Low-temperature thermochronology and
694 thermokinematic modeling of deformation, exhumation and development of 1061 topography
695 in the central Southern Alps, New Zealand. *Tectonics*, 28, TC5011, 1062
696 doi:10.1029/2008TC002367.
- 697 Holloway, J. R. 1984. Graphite-CH₄-H₂O-CO₂ equilibria at low-grade metamorphic
698 conditions. *Geology*, v. 12, p. 455-458.
- 699 Hu, S., Evans, K., Craw, D., Rempel, K., Bourdet, J., Dick, J. & Grice, K. 2015. Raman
700 characterization of carbonaceous material in the Macraes orogenic gold deposit and
701 metasedimentary host rocks, New Zealand. *Ore Geology Reviews* 70: 80-95.
- 702 Huizenga, J-M. 2011. Thermodynamic modelling of a cooling C–O–H fluid–graphite system:
703 implications for hydrothermal graphite precipitation. *Mineralium Deposita*, v. 46, p. 23-33.
- 704 Jenkin, G. R. T., Craw, D. & Fallick, A. E. 1994. Stable isotopic and fluid inclusion evidence
705 for meteoric fluid penetration into an active mountain belt; Alpine Schist, New Zealand.
706 *Journal of Metamorphic Geology* 12, 429–444.

- 707 Jiracek, G. R., Gonzalez, V. M., Caldwell, T. G., Wannamaker, P. E. & Kilb, D. 2007.
708 Seismogenic, electrically conductive, and fluid zones at continental plate boundaries in New
709 Zealand, Himalaya, and California. A Continental Plate Boundary: Tectonics at South Island,
710 New Zealand. *AGU Geophysical Monograph* 175, 347-369.
- 711 Johnstone, R. D., Craw, D. & Rattenbury, M. S. 1990. Southern Alps Cu-Au hydrothermal
712 system, Westland, New Zealand. *Mineralium Deposita* 25 : 118-125.
- 713 Kaneki, S., Hirono, T., Mukoyoshi, H., Sampei, Y., Ikehara, M. 2016. Organochemical
714 characteristics of carbonaceous materials as indicators of heat recorded on an ancient plate-
715 subduction fault. *Geochemistry, Geophysics, Geosystems*, doi: 10.1002/2016GC006368.
- 716 Kleffmann, S., Davey, F. & Melhuish, A. 1998. Crustal structure in the central South Island,
717 New Zealand, from the Lake Pukaki Seismic Experiment. *New Zealand Journal of Geology
718 and Geophysics* 41 (1), 39–49.
- 719 Koons, P. O. 1987. Some thermal and mechanical consequences of rapid uplift: an example
720 from the Southern Alps, New Zealand. *Earth and Planetary Science Letters* 86, 307–319.
- 721 Koons, P. O., Craw, D., Cox, S. C., Upton, P., Templeton, A. S. & Chamberlain, C. P. 1998.
722 Fluid flow during active oblique convergence: a Southern Alps model from mechanical and
723 geochemical observations. *Geology*, 26, 159–162.
- 724 Kribeck, B., Sykorova, I., Machovic, V. & Laufek, F. 2008. Graphitization of organic matter
725 and fluid-deposited graphite in Paleoproterozoic (Birimian) black shales of the Kaya-Goren
726 greenstone belt (Burkina Faso, West Africa). *J Metam Geol* 26: 937-958

- 727 Kuo, L-W., Li, H., Smith, S. A. F. , Di Toro, G., Suppe, J., Song, S-R., Nielsen, S., Sheu, H-
728 S. & Si, J. 2014. Gouge graphitization and dynamic fault weakening during the 2008 Mw 7.9
729 Wenchuan earthquake. *Geology* 42: 47-50.
- 730 Large, R. R., Maslennikov, V. V., Robert, F., Danyushevshy, L. V. & Chang, Z. 2007.
731 Multistage sedimentary and metamorphic origin of pyrite and gold in the giant Sukhoi Log
732 deposit, Lena Gold Province, Russia. *Econ Geol* 105: 1233-1267
- 733 Large, R. R., Bull, S. W. & Maslennikov, V. V. 2011. A carbonaceous sedimentary source-rock
734 model for Carlin-type and orogenic gold deposits. *Econ Geol* 106: 331-358
- 735 Little, T. A., Holcombe, R. J. & Ilg, B. R. 2002. Kinematics of oblique collision and ramping
736 inferred from microstructures and strain in middle crustal rocks, central Southern Alps, New
737 Zealand. *Journal of Structural Geology*, v. 24, p. 219–239, doi:10.1016/S0191-8141(01)00060-
738 8.
- 739 Little, T. A., Cox, S. C. , Vry, J. K. & Batt, G. 2005. Variations in exhumation level and uplift-
740 rate along the oblique-slip Alpine Fault, central Southern Alps, New Zealand. *Geological*
741 *Society of America Bulletin*, 117(5), 707–723.
- 742 Little, T. A., Wightman, R., Holcombe, R. J. & Hill, M. 2007. Transpression models and ductile
743 deformation of the lower crust of the Pacific Plate in the central Southern Alps, a perspective
744 from structural geology, in *A Continental Plate Boundary: Tectonics at South Island, New*
745 *Zealand* edited by D. Okaya, T. Stern, F. Davey. *AGU Geophysical Monograph Series*, 175,
746 271-288.
- 747 Luque, F. J., Pasteris, J. D., Wopenka, B., Rodas, M., & Barrenechea, J. F. 1998. Natural fluid-
748 deposited graphite: mineralogical characteristics and mechanisms of formation. *American*
749 *Journal of Science*, v. 298, p. 471-498.

- 750 Luque, F. J., Ortega, L., Barrenechea, J. F., Millward, D., Beyssac, O. & Huizenga, J-M., (2009)
751 Deposition of highly crystalline graphite from moderate-temperature fluids. *Geology*, v. 37, p.
752 275-278.
- 753 Luque, F. J., Huizenga, J-M., Crespo-Feo, E., Wada, H., Ortega, L. & Barrenechea, J. F. 2014.
754 Vein graphite deposits: geological settings, origins, and economic significance. *Mineralium*
755 *Deposita*, v. 49, p. 261-277.
- 756 Menzies, C. D., Teagle, D. A. H., Craw, D., Cox, S. C., Boyce, A. J., Barrie, C. D. & Roberts,
757 S. 2014. Incursion of meteoric waters into the ductile regime in an active orogen. *Earth and*
758 *Planetary Letters* 399: 1-14
- 759 Nakamura, Y., Oohashi, K., Toyoshima, T., Satish-Kumar, M. & Akai, J. 2015. Strain-induced
760 amorphization of graphite in fault zones of the Hidaka metamorphic belt, Hokkaido, Japan.
761 *Journal of Structural Geology* 72: 142 – 161.
- 762 Norris, R. J., Koons, P. O. & Cooper A. F. (1990) The obliquely convergent plate boundary in
763 the South Island of New Zealand: implications for ancient collision zones, New Zealand.
764 *Journal of Structural Geology*, 12, 715-725.
- 765 Norris, R. J. & Cooper, A. F. 1995. Origin of small scale segmentation and transpressional
766 thrusting along the Alpine fault, New Zealand. *Geological Society of America Bulletin*, v. 107,
767 p. 231–240, doi:10.1130/0016-7606(1995)107 <0231:OOSSSA>2.3.CO;2.
- 768 Norris, R. J. & Cooper, A. F. 2001. Late Quaternary slip rates and slip-partitioning on the
769 Alpine Fault, New Zealand. *Journal of Structural Geology* 23, 507–520.

- 770 Norris, R. J. & Cooper, A. F. 2003. Very high strains recorded in mylonites along the Alpine
771 Fault, New Zealand: implications for the deep structure of plate boundary faults. *Journal of*
772 *Structural Geology* Vol.25(12), pp.2141-2157
- 773 Norris, R. J., & Cooper, A. F. 2007. The Alpine fault, New Zealand: Surface geology and field
774 relationships. *American Geophysical Union Geophysical Monograph* 175, p. 157–175.
- 775 Oohashi, K., Hirose, T., & Shimamoto, T. 2011. Shear-induced graphitization of carbonaceous
776 materials during seismic fault motion: Experiments and possible implications for fault
777 mechanics. *Journal of Structural Geology*, v. 33, p. 1122-1134.
- 778 Parkhurst, D. L. & Appelo, C. A. J. 1999. User's guide to PHREEQC (Version 2) : a computer
779 program for speciation, batch-reaction, one-dimensional transport, and inverse geochemical
780 calculations. *U.S. Geological Survey : Earth Science Information Center, Open-File Reports*
781 *Section [distributor], Water-Resources Investigations Report* 99-4259, xiv, 312 p. :ill. ;28 cm.
- 782 Pasteris, J. D. 1989. In situ analysis in geological thin-sections by laser Raman microprobe
783 spectroscopy: a cautionary note. *Applied Spectroscopy*, 43, 567–570.
- 784 Pitcairn, I. K., Roberts, S., Teagle, D. A. H. & Craw, D. 2005. Detecting hydrothermal graphite
785 deposition during metamorphism and gold mineralisation. *J Geol Soc London* 162: 429-432
- 786 Pitcairn, I. K., Craw, D. & Teagle, D. A. H. 2014. The gold conveyor belt: Large-scale gold
787 mobility in an active orogen. *Ore Geology Reviews* 62, 129-142.
- 788 Reyes, A. G., Christenson, B. W. & Faure, K. 2010. Sources of solutes and heat in low-enthalpy
789 mineral waters and their relation to tectonic setting, New Zealand. *Journal of Volcanology and*
790 *Geothermal Research* 192, 117-141.

- 791 Schleicher, A. M., Sutherland, R., Townend, J., Toy, V. G. & Pluijm, B. A. 2015. Clay mineral
792 formation and fabric development in the DFDP-1B borehole, central Alpine Fault, New
793 Zealand. *Journal of Geology and Geophysics*, DOI: 10.1080/00288306.2014.979841
- 794 Sforza, M., van Zuilen, M. & Philippot, P. 2014. Structural characterization by Raman
795 hyperspectral mapping of organic carbon in the 3.46 billion-year-old Apex chert, Western
796 Australia. *Geochimica et Cosmochimica Acta* 124: 18-33, doi:10.1016/j.gca.2013.09.031
- 797 Sutherland, R., Toy, V. G., Townend, J., Cox, S. C., Eccles, J. D., Faulkner, D. R., Prior, D. J.,
798 Norris, R. J., Mariani, E., Boulton, C., Carpenter, B. M., Menzies, C. D., Little, T. A., Hastings,
799 M., De Pascale, G. P., Langridge, R. M., Scott, H. R., Lindroos, Z. R., Fleming, B. & Kopf, A.
800 J. 2012. Drilling reveals fluid control on architecture and rupture of the Alpine fault, New
801 Zealand. *Geology*, 40(12): 1143-1146; doi: 10.1130/G33614.1
- 802 Toy, V. G., Craw, D., Cooper, A. F., Norris, R. J. 2010. Thermal regime in the central Alpine
803 Fault zone, New Zealand : constraints from microstructures, biotite chemistry and fluid
804 inclusion data. *Tectonophysics*, 485(1-4): 178-192;doi:10.1016/j.tecto.2009.12.013
- 805 Toy, V. G., Ritchie, S. & Sibson, R. 2011. Diverse habitats of pseudotachylytes in the Alpine
806 Fault Zone and relationships to current seismicity. *Geological Society London, Special
807 Publications*, v. 359, p. 115-133, doi: 10.1144/SP359.7
- 808 Toy, V. G., Prior D. J., Norris, R. J., Cooper, A. F. & Walrond, M. 2012. Relationships between
809 kinematic indicators and strain during syn-deformational exhumation of an oblique slip,
810 transpressive, plate boundary shear zone: The Alpine Fault, New Zealand. *Earth and Planetary
811 Science Letters*. Volumes 333–334, p. 282 – 292, doi:10.1016/j.epsl.2012.04.037
- 812 Upton, P., Koons, P. O. & Chamberlain, C. P. 1995. Penetration of deformation-driven meteoric water

- 813 into ductile rocks: isotopic and model observations from the Southern Alps, New Zealand. *New*
814 *Zealand Journal of Geology and Geophysics* 38, 535–543.
- 815 Upton, P. & Craw, D. 2003. Upper crustal fluid flow in the outboard region of the Southern
816 Alps, New Zealand. *Geofluids*, 3, 1–12.
- 817 Upton P. & Craw D. 2008. Modelling the role of graphite in development of a mineralised
818 mid-crustal shear zone, Macraes mine, New Zealand. *Earth Planet Sci Letters* 266: 245-255
- 819 Upton P. & Craw D. 2014. Modelling of structural and lithological controls on mobility of
820 fluids and gold in orogenic belts, New Zealand. In: Garofalo PS, Ridley JR (eds) Gold-
821 Transporting Hydrothermal Fluids in the Earth's Crust. *Geological Society of London Special*
822 *Publication* 402: 231-253.
- 823 Wang L. J. and Chamalaun F. H. 1996. A magnetotelluric traverse across the Adelaide
824 Geosyncline. *Exploration Geophysics* 26: 539 – 546.
- 825 Wannamaker, P. E., Jiracek, G. R., Stodt, J. A., Caldwell, T. G., Gonzalez, V. M., McKnight,
826 D. & Porter, A. D. 2002. Fluid generation and pathways beneath an active compressional
827 orogen, the New Zealand Southern Alps, inferred from magnetotelluric data. *Journal of*
828 *geophysical research*, vol. 107, No. B6, 10.1029/2001JB000186, 2002
- 829 Warr, L. N. & Cox, S. C. 2001. Clay mineral transformations and weakening mechanisms along
830 the Alpine Fault, New Zealand. p. 85-101 IN: Holdsworth, R.E.; Strachan, R.A.; Magloughlin,
831 J.F.; Knipe, R.J. The nature and tectonic significance of fault zone weakening. London.
832 *Geological Society of London special publication* 186.
- 833 Won I. J. 1983. A sweep-frequency electromagnetic exploration method. Chapter 2.
834 *Developments in Geophysical Exploration Methods-4* (AA Fitch, Ed).

- 835 Wopenka, B. & Pasteris, J. D. 1993. Structural characterization of kerogens to granulite-facies
836 graphite: applicability of Raman microprobe spectroscopy. *American Mineralogist* 78, 533–
837 557.